Towards Customized Spatial Resolution in TDLAS Tomography

Towards Customized Spatial Resolution in TDLAS Tomography

Chang Liu, *Member, IEEE*, Stylianos-Alexios Tsekenis, Nick Polydorides, *Member, IEEE* and Hugh McCann

***Abstract*—Tunable diode laser absorption spectroscopy (TDLAS) tomography has been widely employed to spatially and temporally resolve gas parameters in combustion processes. The requirements placed on the spatial resolution of a tomographic image vary in industrial applications, depending on the size of the target field and the necessity to detect small features. Based on an optimized beam arrangement, this work proposes a scheme to customize the spatial resolution in the design of TDLAS tomography systems. To the best of our knowledge, the proposed scheme, for the first time, quantifies the impact on the spatial resolution of varying the number of samples of the imaging space, in both angular and linear dimensions. More importantly, the proposed scheme can be used to determine the most effective optical layout that would achieve a desired spatial resolution. The reduction in the system complexity will enable the sensor to be installed in practical combustors while maintaining reliability. Finally, we apply the proposed scheme in a case study based on experimental data previously acquired from an automotive engine.**

***Index Terms*—tunable diode laser absorption spectroscopy (TDLAS), tomography, beam arrangement, spatial resolution, combustion diagnosis**

I. Introduction

LASER spectroscopic techniques have been extensively applied to combustion diagnostics, enabling better understanding of the turbulence, heat transfer and chemical reactions in the flow fields [1]. Among these techniques, tunable diode laser absorption spectroscopy (TDLAS) provides high speed and high sensitivity using wavelength-tunable laser diodes [2-4]. In the past, line-of-sight TDLAS has been used to retrieve quantitatively the path-averaged temperature, species concentrations, pressure and velocity in reactive flows. To fulfill the increasing demand for monitoring non-uniform and turbulent flow fields, TDLAS is combined with tomographic techniques, namely, TDLAS tomography, which images the aforementioned flow parameters as multi-dimensional distributions [5-7]. Instead of requiring multi-plane optical access to the combustion chamber, TDLAS tomography utilizes pencil-beams on a single optical plane to access the process. Fiber optics are typically used for in-situ studies where optical access is typically hindered by mechanical obstructions [8, 9].

The ability of the tomography system to resolve increasingly smaller features within the region of interest (RoI) determines its applicability to the study of reactive flows. Improvements in spatial resolution have been achieved either physically by denser sampling of the RoI [10] or numerically by data analysis and image processing [11]. Regardless of the data analysis and image reconstruction algorithms, there is a motivation to maximize the number of experimental measurements as this enables optimum performance of the subsequent algorithmic analysis. In laboratory studies where optical access is generous, implementations [12-14] have relied on mechanical means to rotate either the probing laser beams or the RoI. Although these implementations can be used to monitor a stable combustion process, the mass of moving parts places an upper limit to the imaging speed that can be realistically achieved. Among the reported TDLAS tomographic measurements implemented by mechanically moving the laser beam, Wang *et al* maximized the imaging rate to 10 frames/second (fps), to the best of the authors' knowledge, by performing the measurement simultaneously from four platforms that each rotate a single laser beam [12]. However, this in turn precludes such implementations from imaging high-speed flows, e.g. aviation engine exhausts. To overcome this limitation, we recently introduced the concept of solid-state beam deflectors to realize tomographic reconstruction with high temporal and spatial resolution. The laser beam can be deflected through an angle of 216 mrad at a repetition rate of 90 kHz using an electro-optic deflector [15]. Furthermore, stationary TDLAS tomographic sensors have been designed with multi-photodiode arrays [16, 17] or fiber optics [8], in which the spatial resolution is improved by packing around the imaging space the optics for more beams.

In industrial applications, the requirements placed on the spatial resolution of a tomographic image depend on the size of the target combustion field and the size of the smallest feature to be detected. For instance, process control in large-size coal-fired/biomass boilers [18, 19] and thermal power plants [20] requires centimeter-level spatial resolution in the tomographic image, while combustion diagnostics in automotive engines [9, 21] and swirl combustors [17, 22] aim

Manuscript received xx; revised xx; accepted xx. This work was supported by the UK Engineering and Physical Sciences Research Council, via Platform Grant EP/P001661/1, and the University of Edinburgh – Shanghai Jiao Tong University Low Carbon College Seed Grant funding. (Corresponding author: Chang Liu)

C. Liu, S. A. Tsekenis, N. Polydorides, and H. McCann are with the Institute for Digital Communications, School of Engineering, The University of Edinburgh, Edinburgh EH9 3JL, U.K. (e-mail: c.liu@ed.ac.uk).

for millimeter-level spatial resolution. Visualization of the mixing process has been previously demonstrated for both the liquid and vapor phases of fuel injected in the chamber of Spark Ignition (SI) and Compression Ignition (CI) engines [9, 21], however the spatial resolution was insufficient to tomographically resolve the fuel spray pattern. Therefore, a customized spatial resolution is highly demanded for TDLAS tomographic sensor design.

This paper proposes a scheme to customize the spatial resolution with a minimum optical layout. We present an analysis of the influence that the total number of projections and the total number of beams have on the spatial resolution of systems with limited projections. This scheme greatly facilitates the TDLAS tomographic sensor design by satisfying a given spatial resolution using a minimum number of beams and hence cost. We validate this scheme using previous experimental data from an engine fuel injection event. The spatial resolution is tailored to resolve the injection pattern.

II. Methodology

The fundamentals of TDLAS tomography have been well established to reconstruct the 2D distributions of gas parameters [5]. To maximize the effectiveness of the TDLAS tomographic sensor, the beam arrangement should be optimized while maintaining objectivity in assessment of the reconstructed images [23-25]. We quantify and customize the spatial resolution by using the minimum number of beams with appropriately selected linear and angular beam density.

A. TDLAS Tomography

As shown in figure 1, the RoI is discretized into N cells of dimensions $l_c \times l_c$. In each cell, the flow parameters, i.e. the pressure P, the temperature T and the mole fraction of the absorbing species X_{abs} are assumed to be uniform. According to Beer's Law, the integrated absorbance $b_{v,i}$ obtained from the i-th laser beam can be expressed as

$$b_{v,i} = \sum_{j=1}^{N} [PS(T)X_{abs}]_{v,j} l_{ij} \tag{1}$$

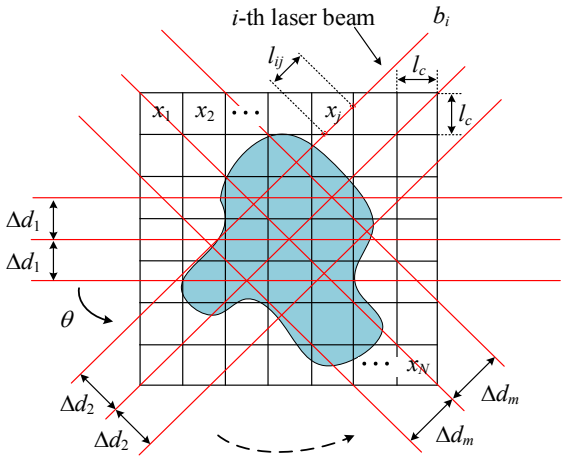

Fig. 1. Geometric description of TDLAS tomography with fixed-view parallel beams and single beam spacing per view.

where i and j are the indices of the laser beams and the cells respectively, and l_{ij} is the absorption path length of the i-th laser beam within the j-th cell. In general, Eqn. (1) can be compactly rewritten as

$$\mathbf{Ax} = \mathbf{b} \tag{2}$$

where $\mathbf{A}$ is the $M \times N$ sensitivity matrix that represents the chord lengths of all the beams within each cell, $\mathbf{x}$ is the $N \times 1$ vector of $[PS(T)X_{abs}]_{v,j}$ to be reconstructed and $\mathbf{b}$ is the $M \times 1$ vector of the sampled $b_{v,i}$.

In practice, optical access to the process is limited, resulting in a rank-deficient problem where Rank($\mathbf{A}$)<N. In this case, $\mathbf{x}$ can be reconstructed by performing the first-order Tikhonov regularization [26] in which the null space of $\mathbf{A}$ is spanned with a smoothing matrix $\mathbf{L}$, defined as

$$\mathbf{L}_{ij} = \begin{cases} 1 & \text{if } i = j \\ -1/k & \text{if } i \text{ neighbours } j \\ 0 & \text{otherwise} \end{cases} \tag{3}$$

where k is the total number of cells neighbouring the i-th cell. As $\mathbf{Lx} = 0$ is satisfied by any uniform $\mathbf{x}$, $\mathbf{x}$ is solved by

$$\mathbf{x}_{\boldsymbol{\lambda}} = \text{argmin} \left\| \begin{bmatrix} \mathbf{A} \\ \lambda \mathbf{L} \end{bmatrix} \mathbf{x} - \begin{bmatrix} \mathbf{b} \\ \mathbf{0} \end{bmatrix} \right\|, s.t. \mathbf{x} \geq 0 \tag{4}$$

where λ is the regularization parameter that balances robustness versus accuracy in the solution.

The Euler equation for Eqn. (4) is

$$(\mathbf{A}^T\mathbf{A} + \boldsymbol{\lambda}\mathbf{L}^T\mathbf{L})\mathbf{x} = \mathbf{A}^T\mathbf{b} \tag{5}$$

and can be solved by

$$\mathbf{x}_{\boldsymbol{\lambda}} = (\mathbf{A}^T\mathbf{A} + \boldsymbol{\lambda}\mathbf{L}^T\mathbf{L})^{-1}\mathbf{A}^T\mathbf{b} \equiv \mathbf{A}^{\#}\mathbf{b} \tag{6}$$

B. Optimization of Beam Arrangement

Given no prior information regarding the distribution, it has been shown that a regular beam array, i.e. equi-angular projections and equi-spaced beams within each projection, leads to uniformly distributing the sampling deficiency across the RoI thus it is preferred over an irregular beam arrangement [23, 25]. Therefore, this work employs the regular beam arrangement and the parameters to be optimized are the beam spacing within each projection (Δd_1, Δd_2, …, Δd_m) and the angular spacing between projections θ. These two parameters are optimized to minimize the fitness value based on the resolution matrix [27].

Assuming the projection data contain a noise-free component $\mathbf{b}^{\text{exact}}$ and a noise-contaminated component $\delta\mathbf{b}$,

$$\mathbf{b} = \mathbf{b}^{\text{exact}} + \boldsymbol{\delta}\mathbf{b} = \mathbf{A}\mathbf{x}^{\text{exact}} + \boldsymbol{\delta}\mathbf{b} \tag{7}$$

Then, Eqn. (6) becomes,

$$\mathbf{x}_{\boldsymbol{\lambda}} = \mathbf{A}^{\#}\mathbf{A}\mathbf{x}^{\text{exact}} + \mathbf{A}^{\#}\boldsymbol{\delta}\mathbf{b} = \mathbf{R}\mathbf{x}^{\text{exact}} + \mathbf{A}^{\#}\boldsymbol{\delta}\mathbf{b} \tag{8}$$

where $\mathbf{R} = \mathbf{A}^{\#}\mathbf{A}$ is the resolution matrix. The reconstruction error is defined as

$$\boldsymbol{\delta}\mathbf{x} = \mathbf{x}_{\boldsymbol{\lambda}} - \mathbf{x}^{\text{exact}} = (\mathbf{R} - \mathbf{I})\mathbf{x}^{\text{exact}} + \mathbf{A}^{\#}\boldsymbol{\delta}\mathbf{b} \tag{9}$$

where $\mathbf{I}$ is the identity matrix. With respect to the rank-deficient problem, $\boldsymbol{\delta}\mathbf{x}$ is dominated by the term $(\mathbf{R}-\mathbf{I})\mathbf{x}^{\text{exact}}$ as the error on solution $\mathbf{x}_{\boldsymbol{\lambda}}$ is less sensitive to $\boldsymbol{\delta}\mathbf{b}$ over a wide range of λ. In this work, λ is fixed at 0.25 so as to keep the same weight for smoothness and accuracy in all reconstructions. Therefore, the beam arrangement should be optimized to minimize the Frobenius norm of $(\mathbf{R}-\mathbf{I})$ given by

$$F(\boldsymbol{\Psi}) = \|\mathbf{R}(\boldsymbol{\Psi}) - \mathbf{I}\|_F^2 \tag{10}$$

where $\boldsymbol{\Psi}$ contains the information of the beam arrangement (Δd_1, Δd_2, …, Δd_m, θ). A genetic algorithm is used in the optimization to find the global minimum value of $F(\boldsymbol{\Psi})$ [27, 28]. The iteration is initiated with 100 randomly generated combinations of $\boldsymbol{\Psi}$. Then, 10 combinations with the lowest $F(\boldsymbol{\Psi})$ are selected to generate the second generation. For each selected combination, 10 children were generated by randomly perturbing the elements in (Δd_1, Δd_2, …, Δd_m, θ) with Gaussian noise. This iteration continues until successive generations yield no further improvement in $F(\boldsymbol{\Psi})$. Given a RoI of 50×50 cells, the optimization progress with for example, 4 projections and 30 beams per projection (referred to as 4×30 hereafter), is monitored by plotting the smallest and average $F(\boldsymbol{\Psi})$ in each generation as can be seen in Figure 2. The iteration stops after the 8th generation, giving an optimized beam layout $\boldsymbol{\Psi}$ with Δd_1=1.69l_c, Δd_2=2.38l_c, Δd_3=1.69l_c, Δd_4=2.38l_c, θ=45°.

C. *Quantification and Customization of Spatial Resolution*

In tomographic application, the smallest feature that can be detected in the RoI is represented by the sharpness of the reconstructed image. As introduced in our previous work [25], the spatial resolution of a tomographic image can be quantified objectively by introducing a sharp-edged inhomogeneity, i.e. a local "step input", and calculating the edge spread function (ESF), i.e. spatial equivalence of "rise-time". As shown in Figure 3 (a), a 2D phantom of gas concentration distribution is created with a sharp-edged rectangular inhomogeneity. As the spatial resolution only as a function of beam layout is studied here, we simplified the tomographic problem by assuming the phantom has uniform distribution of pressure and temperature. Figure 3 (b) shows the reconstruction of the phantom with the optimized beam arrangement, 4×30. With a fixed regularization parameter λ, the rank-deficiency of the TDLAS tomographic problem is the only factor influencing the extent of edge blurring in the tomographic image. Within a rectangular quantification sector as shown by the white outline in Figures 3(a), (b), the linear distance that covers the change of normalized intensity of the ESF from 10% to 90% is defined as the local limiting spatial resolution δ_{sector} as shown in Figure 3 (c).

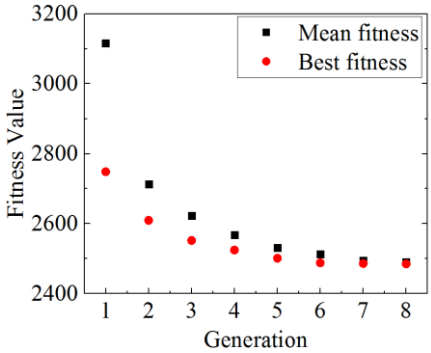

Fig. 2. Monitoring of the fitness in each generation during the beam arrangement optimization for 4×30 using genetic algorithm.

To characterize the global spatial resolution of the tomographic image, the RoI is segmented into a total of 32 quantification sectors at various angular positions on 5 concentric radial tracks, resulting in the segmentation pattern shown in Figure 4 (a). In this way, the spatial resolution in terms of both the linear and angular axes of the sinogram plot can be interrogated. The spatial resolution within each sector is obtained by profiling the ESF when the rectangular inhomogeneity is rotated to the angle with its long edge perpendicular to the long side of the sector. For example, Figures 4 (b)-(e) show the quantification of the local spatial resolution in the 5 sectors on the 2nd track. The inhomogeneity is rotated to the angular positions 0°, 72°, 144°, 216°, and 288° to obtain the spatial resolution, quantitatively and objectively, in the five sectors. The spatial resolution map shown in Figure 5 is obtained when the procedure described above is repeated for all the sectors in all tracks. In this case, the local spatial

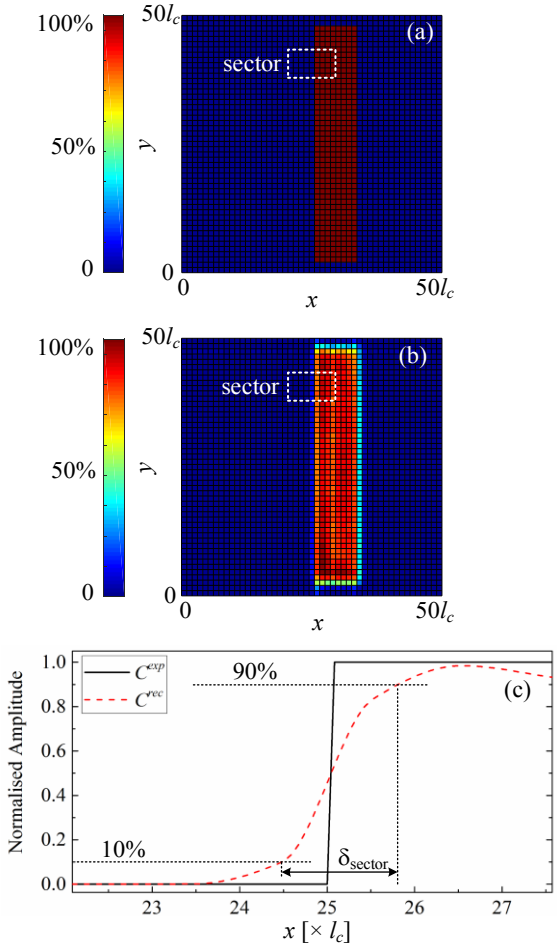

Fig. 3. Quantification of local spatial resolution with the optimized 4×30 beam arrangement. (a) phantom of gas concentration distribution C^{exp} with a sharp-edged rectangular inhomogeneity; (b) reconstructed gas concentration distribution C^{rec}; (c) spatial resolution in the selected sector defined by the linear distance that covers the change of normalized intensity of the edge spread function from 10% to 90%.

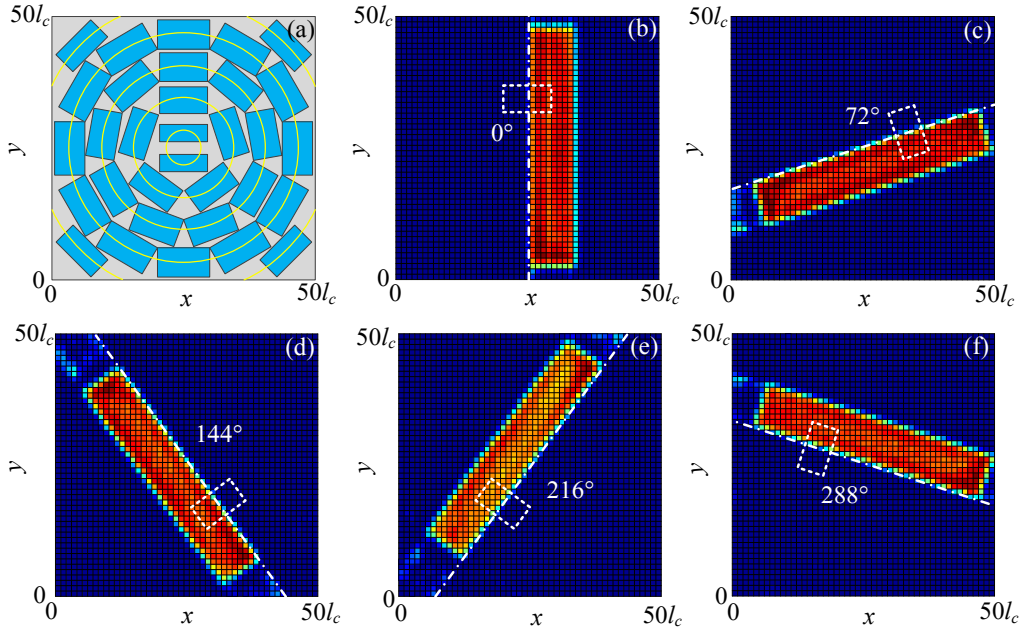

Fig. 4. Quantification of global spatial resolution with optimized beam arrangement 4×30. (a) Segmented RoI with 32 sectors at various angular locations in 5 tracks; (b-f) reconstructions of the rectangular sharp-edged inhomogeneity at 0°, 72°, 144°, 216°, and 288° to obtain the local spatial resolution in the 5 sectors on the 2nd tracks, respectively.

resolution ranges from approx. $0.9l_c$ to $1.7l_c$. The global spatial resolution δ_{global} is defined as the mean value of all the local spatial resolutions in all the sectors, which equals $1.33l_c$ in case of the 4×30 beam arrangement.

The global spatial resolution for other beam arrangements is calculated in the same way and the results shown in Figure 6. Each of these beam arrangements is optimized using the resolution matrix introduced in Section II B. Figure 6 shows how the spatial resolution is influenced by different beam arrangements, initiating TDLAS tomographic sensor design towards the customized spatial resolution in terms of properly laying the laser beams in linear and angular dimensions of the imaging space. The results suggest that, for a fixed total beam count, having more beams per projection (i.e. denser projections) improves the spatial resolution more significantly than having more angular projections. This holds true for four or more angular projections; the spatial resolution deteriorates with three or fewer angular projections irrespective of having more beams per projection. For instance, the δ_{global} achieved by the 8×15 beam arrangement is $2.32l_c$. Given a total of 120 laser beams, δ_{global} decreases monotonically with denser projections but fewer projections, reaching the minimum value of $1.33l_c$ with a 4×30 beam arrangement. However, as stated earlier, further angular under-sampling by a 3×40 beam arrangement results in worsening of the spatial resolution ($1.91l_c$). We can conclude that the excessive angular under-sampling cannot be compensated for by denser linear sampling.

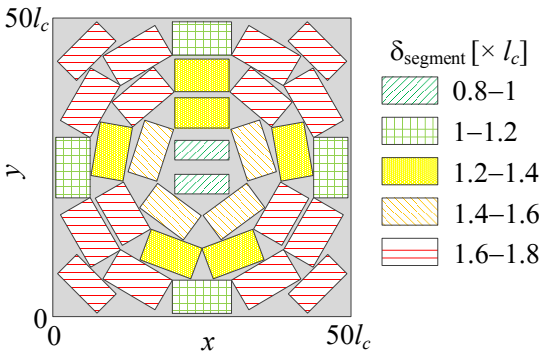

Fig. 5. Spatial resolution map with optimized beam arrangement 4×30, resulting in $\delta_{global} = 1.33l_c$.

The results also enable sensor design to achieve a target spatial resolution with minimal optical layout.The reduction of the optical layout complexity facilitates embedding of the tomographic sensors in combustors with reduced requirements on optical access, making TDLAS tomography more reliable for *in situ* and real-time monitoring of practical combustors at elevated pressures and temperatures.

III. Results and Discussion

In this section the proposed scheme is applied to a TDLAS tomographic sensor design for CI engine diagnostics where

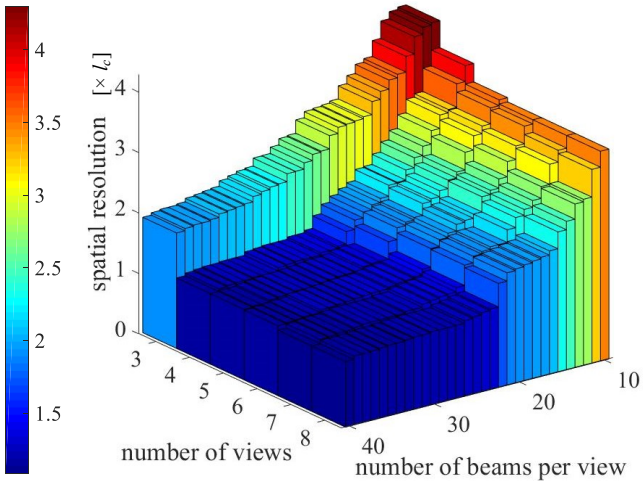

Fig. 6. Dependence of the global spatial resolution on the number of angular views and the number of beams per view.

sufficient spatial resolution is mandatory to image the fuel injection event. Subsequently, we validate the proposed scheme by reconstructing the fuel spray pattern extracted from the tomographic images. Comparing results obtained using different beam layouts having a similar number of beams, the beam arrangement arrived at using our method is shown to be the most efficient solution.

A. Test Platform

Figure 7 (a) depicts the concentration distribution of fuel vapor obtained by Planar Laser-Induced Fluorescence (PLIF) [9]. As PLIF uses a digital camera to capture the 2D target field [29], we assume that the spatial resolution is sufficient to accurately represent the phantom in the tomographic forward problem. Although PLIF can achieve excellent spatial resolution, its implementation requires a high-power and bulky Nd:YAG laser, which typically entails significant safety requirements and typically requires to be operated in a dust free environment. Compared with TDLAS tomography, PLIF is more difficult to apply to practical combustion diagnosis in harsh environments. To facilitate data analysis, the values of gas concentration in the cells are scaled to 0-100%. There are seven distinct high-concentration regions noted $HC_{1\text{-}7}$ in Figure 7 (b) and their centers are projected to the center of the RoI.

The injection pattern is characterized by the location and shape of the high-concentration regions. The location reveals the swirl behavior while the shape denotes mixing of the fuel. As shown in Figure 8 (b), the location is defined by the distance from the centroid for each high-concentration region to the center of the RoI, r_{HC}, and the angular separation from the positive x axis of the RoI, α_{HC}. The shape of the high-concentration region is characterized here simply by its perimeter, p_{HC}, calculated as the number of cells overlapping with the edge of the feature multiplied by the cell width.

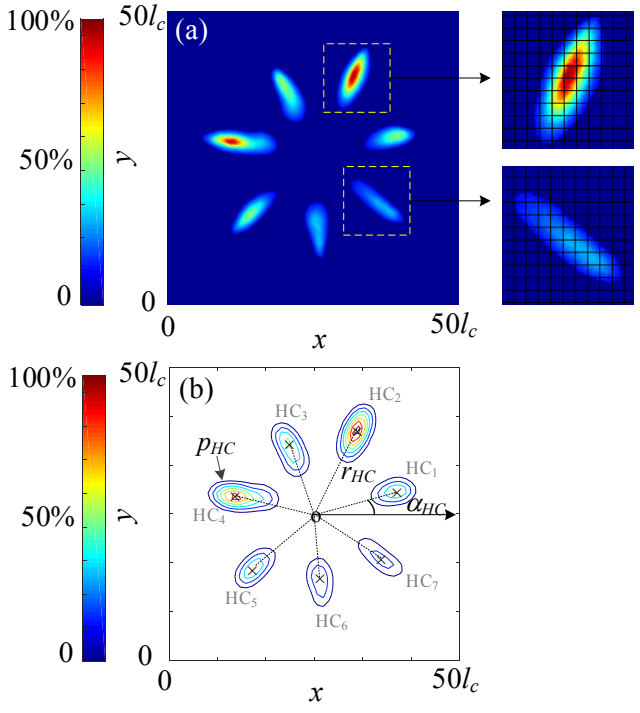

Fig. 7. Distribution of fuel concentration in a CI engine shortly after the start of fuel injection for slow evaporation of lean mixture [9]. (a) Phantom with high spatial resolution captured by PLIF; (b) contours of equal intensity with injection pattern featured by the localisation (e.g. angular α_{HC}, centroid r_{HC}), and shape (e.g. perimeter p_{HC}) of the high-concentration regions.

When characterizing the fuel injection, the fuel distribution should be reconstructed with a clear boundary for each high-concentration region to extract accurately the r_{HC}, α_{HC}, and p_{HC} parameters. As shown in Figure 7 (a), the minimum distance between the peak and boundary values of the high-concentration regions ranges approximately from $1.5l_c$ to $2l_c$. This implies that the tomography system must be capable of resolving inhomogeneities equal to or smaller than $1.5l_c$.

B. Scheme Validation

As shown in Figure 6, the 4×25 beam arrangement can achieve a spatial resolution of $1.41l_c$ (better than the required $1.5l_c$) with a minimum number of projections. The optimized parameters for this layout are (Δd_1=$1.98l_c$, Δd_2=$2.78l_c$, Δd_3=$1.98l_c$, Δd_4=$2.78l_c$, θ=45°). Therefore, the spatial resolution is customized to $1.41l_c$ in this experiment. Figure 8 (a) shows the tomographic image of fuel injection pattern using the 4×25 beam arrangement. The boundary of each high-concentration region is clearly resolved. To evaluate the performance of the tomographic image on reconstructing the injection pattern, parameters r_{HC}, α_{HC}, and p_{HC} for each high-concentration region are evaluated from Figure 8 (a), and compared to the values from the original pattern. As shown in figure 8 (b), the retrieved and actual parameters are in agreement for all high-concentration regions, showing that the tomographic image can effectively represent the features of the

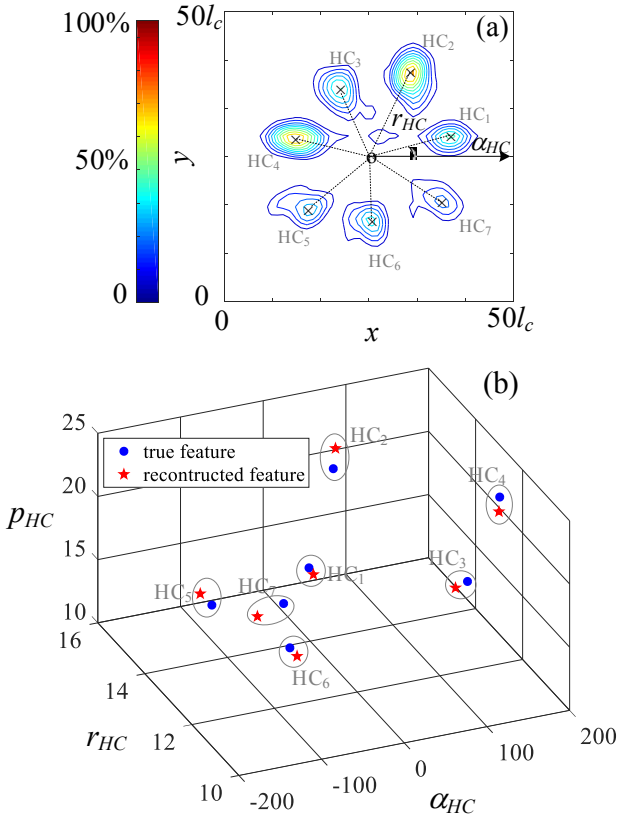

Fig. 8. Image reconstruction of the fuel injection using the customized spatial resolution $1.41l_c$ and the 4×25 beam arrangement. (a) Tomographic image of the phantom shown in Fig. 8 (a); (b) Fuel injection patterns extracted from the reconstructed and the original image.

original fuel injection.

The 4×25 beam arrangement is the most effective way to reconstruct the fuel injection pattern. To verify this result, the fuel injection pattern is also reconstructed using a similar number of total beams but with different beam arrangements. Specifically, we cover the beam arrangements 3×34 (102 beams) and 5×20 (100 beams) corresponding to a spatial resolution of $2.06l_c$ and $1.99l_c$ respectively. The optimized beam layouts $\mathbf{\Psi}$ for 3×34 and 5×20 are (Δd_1=1.44, Δd_2=1.97, Δd_3=1.97, θ=60°) and (Δd_1=2.5, Δd_2=3.49, Δd_3=3.15, Δd_4=3.15, Δd_5=3.49, θ=36°) respectively. As shown in Figure 9, the boundaries of the high-concentration regions are blurred and distorted due to the inadequate spatial resolution. Regions of significant overlap can be seen between HC_2/HC_3, HC_5/HC_6 for the 3×34, and HC_2/HC_3 for the 5×20. Such overlaps can lead to false recognition of the fuel injection pattern. These arrangements are therefore unsuitable to image the test pattern in this work. With *a priori* information, such as the threshold values of each high-concentration region and the gap between the neighbouring regions, the post image processing will indeed help in recovering the features if the ambiguous images suffer from overlap between the high-concentration regions. However, the proposed method is more robust when *a priori* information is not available. An acceptable tomographic image obtained using the customized spatial resolution will also significantly save on computation cost, facilitating the realization of real-time TDLAS tomography on a low-cost system-on-chip.

C. Discussion

In practice, the projection data are always contaminated with noise, which may arise from flow-field-induced beam steering, laser power fluctuations or noise sources within the photo-detection circuit. To examine the proposed scheme for noise-contaminated data, we added random noise to the noise-free data. Using the customized spatial resolution of $1.41l_c$ and the 4×25 beam arrangement, Figure 10 shows the reconstructed images of the fuel injection event with 2%, 5% and 8% random noise added to the measurements. Image quality deteriorates as the noise level increases. Nevertheless, all of the seven high-concentration regions are unambiguously resolved even with 8% noise. This suggests that the customized spatial resolution of $1.41l_c$ is still valid for feature extraction with the noise-contaminated data.

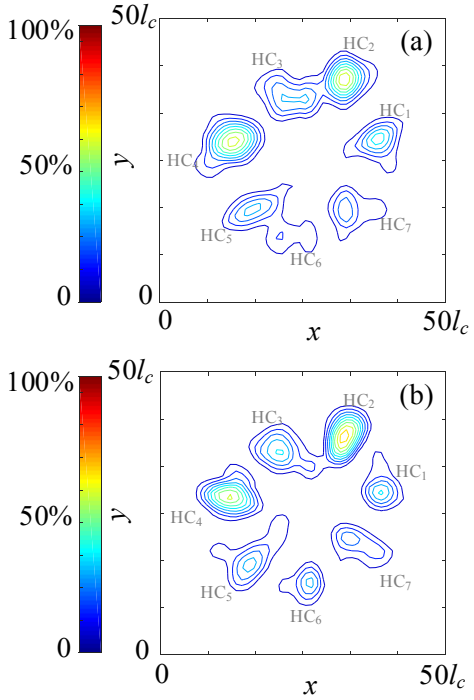

Fig. 9. Image reconstruction of the fuel injection using (a) 3×34 and (b) 5×20 beam arrangements.

IV. Conclusions

In response to the need for detecting small features in industrial applications, this work proposed a scheme to customize the spatial resolution for TDLAS tomography. This study adopted regular beam arrays having equi-angular projections and uniform parallel beam spacing within each projection. To maximize objectivity in assessing the reconstructed images, each beam arrangement was optimized in terms of angular and linear dimensions using the resolution

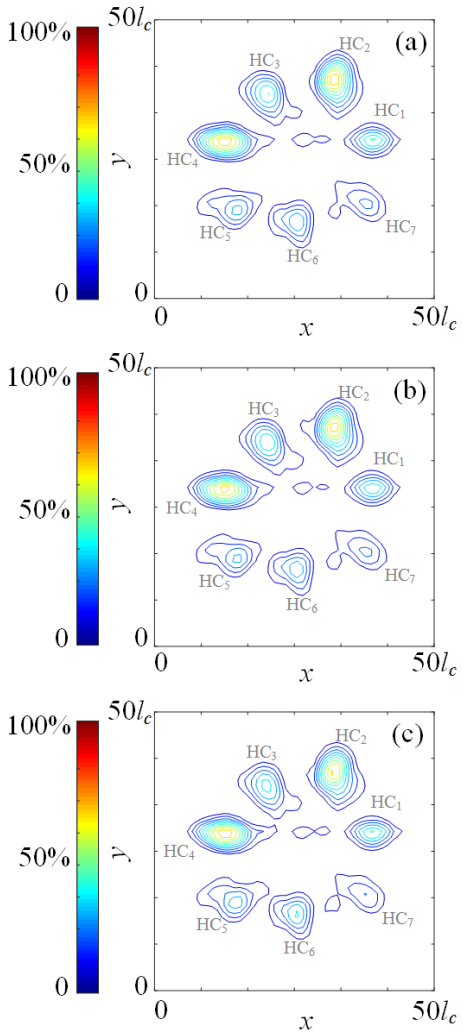

Fig. 10. Image reconstruction of the fuel injection using 4×25 beam arrangement when (a) 2%, (b) 5% and (c) 8% random noises are added on the measurements.

matrix. Based on the systematic and objective quantification of spatial resolution, a map of the spatial resolution was obtained as a function of the different beam arrangements. To the best of our knowledge, the proposed scheme, for the first time, reveals quantitatively the impact of introducing denser linear and angular projections on improving the spatial resolution, and therefore initiates the design of practical TDLAS tomographic sensors that achieve a desired spatial resolution with minimum optical layout complexity.

The proposed scheme was applied to CI engine fuel distribution data obtained by PLIF and validated by simulated tomographic reconstruction of the fuel injection pattern. According to the requirement of resolving the feature with the minimum dimension larger than $1.5l_c$, the spatial resolution was customized to $1.41l_c$ and achieved using a 4×25 beam arrangement. The tomographic image based on the customized spatial resolution faithfully represents the original fuel injection pattern. Compared with systems having a similar total number of beams in 3×34 and 5×20 beam arrangements, the 4×25 beam arrangement is the most cost-effective solution for both noise-free and noise-contaminated measurements. The results indicate the proposed scheme of customizing the spatial resolution also guides a cost-effective beam arrangement for tomographic imaging of the fuel distribution in CI engines. It is worth noting that the numerical results obtained here hold out the prospect of achieving spatial resolution of 3 mm or less, for a typical automotive engine with cylinder bore approx. 80 mm, and an optimized layout of 100 beams. This is to be compared with values of about 8 mm when 30 beams were deployed in a less prescriptive manner [25]. The proposed scheme can be extended to other applications where physical constraints prevent dense image space sampling, such as combustion diagnosis of boilers and power plants.

REFERENCES

[1] R. K. Hanson, R. M. Spearrin, and C. S. Goldenstein, *Spectroscopy and Optical Diagnostics for Gases*: Springer International Publishing, 2016.

[2] C. S. Goldenstein, R. M. Spearrin, J. B. Jeffries, and R. K. Hanson, "Infrared laser-absorption sensing for combustion gases," *Progress in Energy and Combustion Science,* vol. 60, pp. 132-176, 2017.

[3] M. A. Bolshov, Y. A. Kuritsyn, and Y. V. Romanovskii, "Tunable diode laser spectroscopy as a technique for combustion diagnostics," *Spectrochimica Acta Part B: Atomic Spectroscopy,* vol. 106, pp. 45-66, 2015.

[4] C. Liu, and L. Xu, "Laser absorption spectroscopy for combustion diagnosis in reactive flows: A review," *Applied Spectroscopy Reviews*, pp. 1-44, 2018.

[5] H. McCann, P. Wright, and K. Daun, "Chemical Species Tomography," *Industrial Tomography: Systems and Applications*, M. Wang, ed., pp. 135-174, Cambridge, UK: Woodhead Publishing, 2015.

[6] W. Cai, and C. F. Kaminski, "Tomographic absorption spectroscopy for the study of gas dynamics and reactive flows," *Progress in Energy and Combustion Science,* vol. 59, pp. 1-31, 2017.

[7] T. York, H. McCann, and K. B. Ozanyan, "Agile Sensing Systems for Tomography," *IEEE Sensors Journal,* vol. 11, no. 12, pp. 3086 -3105, 2011.

[8] P. Wright, N. Terzija, J. L. Davidson, S. Garcia-Castillo, C. Garcia-Stewart, S. Pegrum, S. Colbourne, P. Turner, S. D. Crossley, T. Litt, S. Murray, K. B. Ozanyan, and H. McCann, "High-speed chemical species tomography in a multi-cylinder automotive engine," *Chemical Engineering Journal,* vol. 158, no. 1, pp. 2-10, 2010.

[9] S.-A. Tsekenis, K. G. Ramaswamy, N. Tait, Y. Hardalupas, A. Taylor, and H. McCann, "Chemical species tomographic imaging of the vapour fuel distribution in a compression-ignition engine," *International Journal of Engine Research*, pp. 1468087417730214, 2017.

[10] M. P. Wood, and K. B. Ozanyan, "Concentration and temperature tomography at elevated pressures," *IEEE Sensors Journal,* vol. 13, no. 8, pp. 3060-3066, 2013.

[11] D. M. Scott, and H. McCann, *Process Imaging for Automatic Control*, Boca Raton, FL, USA: CRC Press, 2005.

[12] F. Wang, K. F. Cen, N. Li, J. B. Jeffries, Q. X. Huang, J. H. Yan, and Y. Chi, "Two-dimensional tomography for gas concentration and temperature distributions based on tunable diode laser absorption spectroscopy," *Measurement Science & Technology,* vol. 21, no. 4, pp. 045301(10pp), 2010.

[13] V. Kasyutich, and P. Martin, "Towards a two-dimensional concentration and temperature laser absorption tomography sensor system," *Applied Physics B: Lasers and Optics,* vol. 102, no. 1, pp. 149-162, 2011.

[14] J. Foo, and P. A. Martin, "Tomographic imaging of reacting flows in 3D by laser absorption spectroscopy," *Applied Physics B,* vol. 123, no. 5, pp. 160, 2017.

[15] S. A. Tsekenis, and N. Polydorides, "Optical access schemes for high speed and spatial resolution optical absorption tomography in energy engineering," *IEEE Sensors Journal,* vol. 17, no. 24, pp. 8072-8080, 2017.

[16] W. Jing, Z. Cao, H. Zhang, Q. Qu, and L. Xu, "A Reconfigurable Parallel Data Acquisition System for Tunable Diode Laser Absorption Spectroscopy Tomography," *IEEE Sensors Journal,* vol. 17, no. 24, pp. 8215-8223, 2017.

[17] C. Liu, Z. Cao, Y. Lin, L. Xu, and H. McCann, "Online Cross-Sectional Monitoring of a Swirling Flame Using TDLAS Tomography," *IEEE Transactions on Instrumentation and Measurement,* vol. 67, no. 6, pp. 1338-1348, 2018.

[18] A. D. Sappey, P. Masterson, E. Huelson, J. Howell, M. Estes, H. Hofvander, and A. Jobson, "Results of closed-loop coal-fired boiler operation using a TDLAS sensor and smart process control software," *Combustion Science and Technology,* vol. 183, no. 11, pp. 1282-1295, 2011.

[19] Z. Qu, P. Holmgren, N. Skoglund, D. R. Wagner, M. Broström, and F. M. Schmidt, "Distribution of temperature, H2O and atomic potassium during entrained flow biomass combustion – Coupling in situ TDLAS with modeling approaches and ash chemistry," *Combustion and Flame,* vol. 188, no. Supplement C, pp. 488-497, 2018.

[20] Y. Deguchi, T. Kamimoto, Z. Z. Wang, J. J. Yan, J. P. Liu, H. Watanabe, and R. Kurose, "Applications of laser diagnostics to thermal power plants and engines," *Applied Thermal Engineering,* vol. 73, no. 2, pp. 1453-1464, 2014.

[21] N. Terzija, S. Karagiannopoulos, S. Begg, P. Wright, K. Ozanyan, and H. McCann, "Tomographic imaging of the liquid and vapour fuel distributions in a single-cylinder direct-injection gasoline engine," *International Journal of Engine Research,* vol. 16, no. 4, pp. 565-579, 2015.

[22] C. Liu, Z. Cao, F. Li, Y. Lin, and L. Xu, "Flame monitoring of a model swirl injector using 1D tunable diode laser absorption spectroscopy tomography," *Measurement Science and Technology,* vol. 28, no. 5, pp. 054002, 2017.

[23] D. McCormick, M. G. Twynstra, K. J. Daun, and H. McCann, "Optimising laser absorption tomography beam arrays for imaging chemical species in gas turbine engine exhaust plumes."

[24] T. Yu, B. Tian, and W. Cai, "Development of a beam optimization method for absorption-based tomography," *Optics Express,* vol. 25, no. 6, pp. 5982-5999, 2017.

[25] S. A. Tsekenis, N. Tait, and H. McCann, "Spatially resolved and observer-free experimental quantification of spatial resolution in tomographic images," *Review of Scientific Instruments,* vol. 86, no. 3, pp. 035104, 2015.

[26] K. J. Daun, "Infrared species limited data tomography through Tikhonov reconstruction," *Journal of Quantitative Spectroscopy and Radiative Transfer,* vol. 111, no. 1, pp. 105-115, 2010.

[27] M. G. Twynstra, and K. J. Daun, "Laser-absorption tomography beam arrangement optimization using resolution matrices," *Appl. Opt.,* vol. 51, no. 29, pp. 7059-7068, 2012.
[28] M. P. Wood, and K. B. Ozanyan, "Simultaneous temperature, concentration, and pressure imaging of water vapor in a turbine engine," *Sensors Journal, IEEE,* vol. 15, no. 1, pp. 545-551, 2015.
[29] C. Schulz, and V. Sick, "Tracer-LIF diagnostics: quantitative measurement of fuel concentration, temperature and fuel/air ratio in practical combustion systems," *Progress in Energy and Combustion Science,* vol. 31, no. 1, pp. 75-121, 2005.

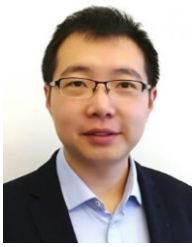

Chang Liu (M'18) received the B.Sc. degree in automation from Tianjin University, Tianjin, China in 2010; the Ph.D. degree in testing, measurement technology and instrument in Beihang University, Beijing, China, in 2016. From April 2016 to January 2018, he was a postdoctoral researcher in the department of air pollution and environmental technology, Empa-Swiss Federal Laboratories for Materials Science and Technology, Dübendorf, Switzerland. From February 2018, he is a lecturer in the School of Engineering, University of Edinburgh, Edinburgh, UK. His current research interests include NIR/MIR laser absorption spectroscopy (LAS), LAS tomographic technique and system design, and their applications to combustion diagnostic and trace gas sensing.

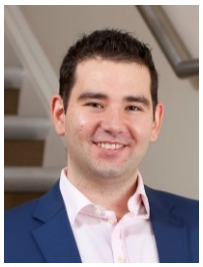

Stylianos-Alexios Tsekenis received the BEng and EngD degrees in electrical and electronic engineering from the University of Manchester, UK in 2009 and 2013 respectively. He received the Pg.Dip degree in Enterprise management from Manchester Business School in 2011. He has held posts at Intel Corporation, Royal Dutch Shell plc. and Blaupunkt GmbH, developing instrumentation systems that are now in world-wide use. As is a Chartered Engineer and a Certified Associate in Project Management, he has provided technology and be-spoke design consultancy services to the events and motorsport industries. He is the co-founder of an electronic product design company. In 2014, he joined the Agile Tomography Group at the University of Edinburgh, UK as a Research Associate. His current R&D interests are optical tomography systems to image the spatio-temporal distribution of gases. The systems are used to advance automotive, marine and aero engine technologies in order to reduce emissions and optimize energy efficiency.

Nick Polydorides (M'09) received the B.Eng. degree in electrical and electronic engineering from the University of Manchester Institute of Science and Technology, Manchester, U.K., in 1998; the M.Sc. degree in computation from the University of Oxford, Oxford, U.K., in 1999; and the Ph.D. degree in electrical tomography from The University of Manchester, Manchester, in 2002. He held postdoctoral positions with the School of Mathematics, The University of Manchester, and with the Laboratory for Information and Decision Systems, Massachusetts Institute of Technology, Cambridge, MA, USA. In 2010, he was with The Cyprus Institute, Nicosia, Cyprus, as an Assistant Professor. He is currently a Senior Lecturer with the Institute of Digital Communications, School of Engineering, The University of Edinburgh, U.K.

Hugh McCann received the B.Sc. and Ph.D. degrees from the University of Glasgow, Glasgow, U.K., in 1976 and 1980, respectively. He was appointed Professor of Tomographic Imaging at The University of Edinburgh, Edinburgh, Scotland, U.K., in 2013 and Head of the School of Engineering 2013-18. From 1996 to 2013, he was Professor of Industrial Tomography at the University of Manchester, Manchester, U.K., following ten years in R&D at the Royal Dutch/Shell Group. He was involved in high-energy particle physics for ten years at Glasgow, Manchester, CERN (Geneva, Switzerland) and DESY (Hamburg, Germany). He has extended industrial tomography to provide specific chemical contrast using high-speed all-opto-electronic techniques, and has developed electrical impedance tomography for medical applications, collaborating intensively with users in both academia and industry. He was Head of the School of Electrical and Electronic Engineering, Manchester, from 1999 to 2002, the Chair of the U.K. Professors and the Head of Electrical Engineering from 2003 to 2005, and of the Virtual Centre for Industrial Process Tomography from 2005 to 2009. Prof. McCann was elected a Fellow of the Royal Academy of Engineering in 2009 and a Fellow of the Royal Society of Edinburgh in 2015.